

# A search for pair halos around active galactic nuclei through a temporal analysis of *Fermi*-LAT data

D. A. Prokhorov<sup>1</sup> \* and A. Moraghan<sup>2,3</sup> †

<sup>1</sup> Department of Physics and Electrical Engineering, Linnaeus University, 351 95 Växjö, Sweden

<sup>2</sup> Academia Sinica Institute of Astronomy and Astrophysics, P.O. Box 23-141, Taipei 106, Taiwan

<sup>3</sup> Center for Galaxy Evolution Research and Department of Astronomy, Yonsei University, Seoul 120-749, Republic of Korea

26 May 2022

## ABSTRACT

We develop a method to search for pair halos around active galactic nuclei (AGN) through a temporal analysis of  $\gamma$ -ray data. The basis of our method is an analysis of the spatial distributions of photons coming from AGN flares and from AGN quiescent states and a further comparison of these two spatial distributions. This method can also be used for a reconstruction of a point spread function (PSF). We found no evidence for a pair halo component through this method by applying it to the *Fermi*-LAT data in the energy bands of 4.5-6, 6-10, and  $>10$  GeV and set upper limits on the fraction of photons attributable to a pair halo component. An illustration of how to reconstruct the PSF of *Fermi*-LAT is given. We demonstrate that the PSF reconstructed by using this method is in good agreement with that which was obtained by using the  $\gamma$ -ray data taken by LAT in the direction of the Crab pulsar and nebula.

**Key words:** gamma-rays: general, galaxies: active, methods: data analysis, intergalactic medium

## 1 INTRODUCTION

The existence of possible extended, diffuse,  $\gamma$ -ray sources (so-called pair halos) around active galactic nuclei (AGNs) was predicted by Aharonian et al. (1994).  $\gamma$  rays with energies above  $\sim 1$  TeV emitted by distant AGNs cannot propagate over cosmological distances because of electron-positron pair production ( $\gamma + \gamma \rightarrow e^- + e^+$ ) on the optical/infrared extragalactic background light (EBL, see, e.g., Kneiske et al. 2002; Franceschini et al. 2008; Finke et al. 2010). The electron-positron pairs created in the  $\gamma$ - $\gamma$  interactions travel in the intragalactic magnetic field and emit secondary cascade  $\gamma$  rays with energies  $\sim 1$  GeV owing to inverse Compton (IC) scattering by cosmic microwave background (CMB) photons. Thus, a  $\gamma$ -ray image of an AGN is expected to exhibit a halo of secondary photons around a central point-like source. A potential detection of pair halos around AGNs will provide us with a measurement of the strength of the intergalactic magnetic field (for a review, see Neronov & Semikoz 2009). The existence of this weak “seed” magnetic field itself is unavoidable because this is required for the production of magnetic fields in galaxies and in clusters of galaxies which are about  $10^{-6}$  gauss via

field amplification mechanisms (for a review, see Ryu et al. 2012).

The *Fermi* Large Area Telescope (LAT) is a pair conversion telescope designed to cover the broad energy range from 20 MeV to greater than 300 GeV (Atwood et al. 2009). The broad energy range of *Fermi*-LAT, therefore, covers typical energies of secondary IC photons if the energies of primary  $\gamma$  rays are between  $\simeq 1$  and  $\simeq 20$  TeV. The *Fermi*-LAT normally operates in sky-survey mode where the whole sky is observed every 3 hr and *Fermi*-LAT sensitivity allows us to monitor AGNs on a daily basis. This quality of *Fermi*-LAT data is particularly important to search for  $\gamma$ -ray flares of AGNs. The second catalog of high-energy  $\gamma$ -ray sources (the 2FGL catalog, Nolan et al. 2012) detected by *Fermi*-LAT and derived from data taken during the first 2 years of the *Fermi* mission was released by the *Fermi*-LAT collaboration. The 2FGL catalog contains 1873 sources detected and characterised in the 100 MeV to 100 GeV range of which 127 are firmly identified and 1171 are reliably associated with counterparts of known or likely  $\gamma$ -ray producing source classes. Note that the 2FGL catalog contains 1047  $\gamma$ -ray sources associated with AGNs, mostly blazars, and, therefore, this source class is dominant in the catalog. Since AGNs are extragalactic sources, AGNs are almost uniformly distributed on the  $\gamma$ -ray sky. This property will allow us to select a sample of AGNs that are not projected on the Galactic

\* E-mail: phdmitry@gmail.com

† E-mail: ajm@asiaa.sinica.edu.tw

plane and, therefore, this sample will be less contaminated by Galactic  $\gamma$ -ray emission.

Pair halos have not yet been detected through a stacking analysis of AGN images in *Fermi*-LAT data (Neronov et al. 2011; Ackermann et al. 2013). However, an important and continuous work by the *Fermi*-LAT team on  $\gamma$ -ray event reconstruction leads to better understanding the performance of the LAT instrument. The continuous accumulation of the data by the LAT improves the sensitivity in the search for pair-halos. Meanwhile, a non-detection of pair halos has put important limits on the intergalactic magnetic field,  $B \geq 10^{-16} - 10^{-15}$  gauss through non-observations of GeV emission from TeV blazars (Neronov & Vovk 2010; Tavecchio et al. 2010; Dolag et al. 2011). Note that the value of intergalactic magnetic field strength has not been measured by any approach and that  $\gamma$ -ray astronomy provides us with promising methods to measure this magnetic field strength even possibly in the near future (see Neronov & Semikoz 2009). Apart from a direct search of the extension of  $\gamma$ -ray emission around AGNs, there are independent and complementary methods to probe the intergalactic magnetic field using  $\gamma$ -ray data, including a search for time delays in  $\gamma$ -ray flares (see Plaga 1995; Murase et al. 2008), studies based on spectral data alone (Essey et al. 2011), or observations of astronomical events such as solar occultations of blazar 3C 279 (Fairbairn et al. 2010)<sup>1</sup>.

The importance of a careful point spread function (PSF) reconstruction from the on-orbit *Fermi*-LAT data was emphasized by Ando & Kusenko (2010) and Neronov et al. (2011). Neronov et al. (2011) compared the stacked AGN signal to the signal of the Crab pulsar and nebula, which is a bright galactic gamma-ray source, and found that the shapes of the two signals coincide. This means that the entire stacked AGN signal is well described by a point-source signal. A detailed analysis by Ackermann et al. (2013) showed that the PSF determined from two years of on-orbit data above 3 GeV is found to be broader than the pre-launch PSF determined through extensive Monte Carlo simulations and beam tests (this agrees well with the results by Neronov et al. (2011)). To calibrate the PSF, they adopted a technique of stacking sources, where the angular offsets of  $\gamma$  rays from their presumed sources are analyzed as if they came from a single source. Pulsars would be ideal for calibrating the PSF. However, the  $\gamma$  rays from pulsars above 10 GeV are limited. They selected a subset of 65 AGNs to calibrate the PSF. Out of the 65 sources, 35 were associated with BL Lac-type blazars, 27 with Flat Spectrum Radio Quasars (FSRQ), 1 with a non-blazar active galaxy, and 2 with an active galaxy of uncertain type. Ackermann et al. (2013) estimated the 68% containment radii for front and

back events from the Geminga and Vela pulsars below 31.6 GeV and the AGN calibration data set above 3.16 GeV. Using the pulsed  $\gamma$ -ray emission between 1 GeV to 31.6 GeV from pulsars, which appears as a true point source to the *Fermi*-LAT, they placed limits on the angular extension of AGN emission relative to pulsar emission and derived the upper limits for the fraction of  $\gamma$  rays from the stacked AGN sample attributable to a pair halo component.

In this paper, we develop a method to reconstruct the PSF and to search for pair halos through a temporal analysis of AGN emission. We illustrate its application to *Fermi*-LAT data. The  $\gamma$ -ray emission of AGN can be divided into three components, which are  $\gamma$ -ray flares, quiescent  $\gamma$ -ray emission from a compact region around AGNs, and extended pair halo emission. The first component is strongly variable in time, while the pair halo component is time-invariant. Numerous flares from AGNs were detected with *Fermi*-LAT<sup>2</sup> (Abdo et al. 2010b). Thus, for example, an active galaxy 3C 454.3 located 7.2 billion light-years away, was the brightest source in the gamma-ray sky during its strong gamma-ray flaring activity<sup>3</sup> (Ackermann et al. 2010). A typical duration of flares, which range from a few days to several weeks, indicates that the spatial region where a flare takes place is less than 1 pc (i.e.,  $c \times \Delta t$ , where  $c$  is the speed of light and  $\Delta t$  is a duration of a flare). During episodes of strong  $\gamma$ -ray flares, AGNs are true point sources to the *Fermi*-LAT and the fluxes of the first component strongly exceed the contribution of the second and third components. Below, we study the  $\gamma$ -ray AGN emission during flares and quiescent states to reconstruct the *Fermi*-LAT PSF and to perform a search for a pair halo component which might contribute to quiescent AGN emission.

## 2 OBSERVATIONS WITH FERMI-LAT AND DATA REDUCTION

The Fermi satellite was launched on 2008 June 11 into a nearly circular Earth orbit with an altitude of 565 km, an inclination of 25.6°, and an orbital period of 96 minutes. The principal instrument on Fermi is the LAT (Atwood et al. 2009), a pair-production telescope with a large effective area ( $\sim 8000$  cm<sup>2</sup> at 1 GeV) and field of view (2.4 sr). The energy range of LAT sensitivity spans from 20 MeV to  $>300$  GeV with an angular resolution per single event of approximately  $\approx 5^\circ$  at 100 MeV and narrowing to  $\approx 0.8^\circ$  at 1 GeV, and to  $\approx 0.15^\circ$  at 10 GeV. The LAT tracker has 12 layers of 3% radiation length tungsten converters (front section), followed by 4 layers of 18% radiation length tungsten converters (back section). The front and back sections have intrinsically different PSF due to multiple scattering with the PSF for front-converting events being approximately a factor of two better than the PSF for back-converting events (e.g., an angular resolution per single front-converting event of approximately  $\approx 0.6^\circ$  at 1 GeV and per single back-converting event of approximately  $\approx 1^\circ$  at 1 GeV). After the commissioning phase, the Fermi-LAT began routine science operations on 2008 August 4. The Fermi-LAT normally

<sup>1</sup> Note that the Sun is a bright extended gamma-ray source. The solar gamma-ray flux is not small compared with that of 3C 279 (at least during the solar cycle minimum). The emission from the solar disk is due to the cosmic-ray cascades in the solar atmosphere and the largely extended emission around the Sun is due to the inverse Compton scattering of cosmic-ray electrons off solar photons (Abdo et al. 2011). This along with the short duration of occultations significantly complicate a search of a pair halo around 3C 279 during solar occultations (Barbiellini et al. 2014; Kotelnikov et al. 2015).

<sup>2</sup> [http://fermi.gsfc.nasa.gov/ssc/data/access/lat/msl\\_1c/](http://fermi.gsfc.nasa.gov/ssc/data/access/lat/msl_1c/)

<sup>3</sup> Most of the time, the brightest source in the gamma-ray sky is the Vela pulsar.

operates in sky-survey mode which provides a full-sky coverage every 3 hours (i.e., 2 orbits).

We downloaded the Pass 7 Reprocessed Fermi-LAT data from the Fermi Science Support Center<sup>4</sup>. Note that the Pass 7 Reprocessed Fermi dataset uses updated calibration constants (Bregeson et al. 2013). The primary differences with respect to the Pass 7 data are the correction of a slight (1% per year) expected degradation in the Calorimeter light yield and significant improvement of the Calorimeter position reconstruction, which in turn significantly improves the LAT point-spread function at high energies ( $>5$  GeV)<sup>5</sup>. For the data analysis, we use the Fermi Science Tools v9r32p5 package<sup>6</sup> and P7REP instrument response functions (IRFs). The improved position reconstruction of  $\gamma$ -ray events above 5 GeV is useful in the search for pair halos using the Pass 7 Reprocessed Fermi-LAT data at these energies.

We used the Fermi LAT 2-year point source catalog (Nolan et al. 2012), `gll_psc_v08.fit`, to select the sample of AGNs for our analysis. Firstly, we recorded the source type of all 2FGL sources and selected sources associated with AGNs. To reduce the contamination by the Galactic diffuse foreground emission to the regions of interest, we excluded AGNs with Galactic latitude between  $-30^\circ$  to  $30^\circ$ . To reduce the contamination the regions of interest by 2FGL  $\gamma$ -ray sources, we excluded AGNs which have neighboring (2FGL) sources within  $2^\circ$ . At this stage, our sample contains 394  $\gamma$ -ray AGNs. We began by selecting all gamma rays of energy above 1 GeV within a  $4^\circ$  radius around the direction of each AGN (the positions of AGNs taken from the 2FGL catalog (Nolan et al. 2012)), and satisfying the SOURCE event class. For this analysis, we have accumulated events obtained from 2008 August 4 to 2013 November 7 (i.e., 5.2 years of the *Fermi*-LAT data), corresponding to 239557417 and 405478386 in units of the Mission Elapsed Time. To reduce the contamination by the  $\gamma$ -ray emission coming from cosmic-ray interactions in the Earth's upper atmosphere (so-called albedo  $\gamma$  rays) our selection is refined by choosing events with zenith angles  $<100^\circ$ . We removed events that occur during satellite maneuvers when the LAT rocking angle was larger than  $52^\circ$ . Time intervals when some event has negatively affected the quality of the LAT data are also excluded. Both the front-converting and back-converting events are selected. Note that the statistics are higher when we consider both the front-converting and back-converting events together. To justify the usage of the front-converting and back-converting events together for the increase of statistics, below we will compute the ratio of the numbers of front-to-back events recorded during quiescent AGN states and recorded during AGN flares, respectively, and will compare these ratios to make sure that they are consistent within the error bars. Below we show that the accumulation of the *Fermi*-LAT data during 5.2 years made possible the reconstruction of the PSF (see Sect. 4.2) and the search for potential pair-halo extended emission (see Sect.

3.2) by applying the technique based on a study of quiescent and flaring AGN states.

### 3 TEMPORAL ANALYSIS FOR A SEARCH FOR PAIR HALOS AROUND AGNS

To disentangle AGN flares from quiescent AGN emission states, we perform a temporal analysis of the *Fermi*-LAT data. Below, we will compare the spatial distribution of photons coming during AGN flare episodes with that of photons coming during quiescent AGN states. This will allow us to set the 95% upper limits on the fraction of  $\gamma$  rays attributable to a pair halo component. To perform this analysis, we will determine  $\gamma$ -ray flares for each AGN from our sample of 394 AGNs and calculate the distribution of photons into annular bins for AGN flares and for quiescent AGN states.

To disentangle AGN flares from quiescent AGN emission states, we define an AGN flare in a statistical way. We determine flares in the Poisson regime. The Poisson distribution expresses the probability of a given number of events occurring in a fixed interval of exposure assuming these events occur with the same average rate. During AGN flare episodes, the flux from an AGN increases compared with its quiescent state. To improve the strength of the selection of flares, we calculate the total number of photons coming within the circle with a radius of  $1^\circ$  above 1 GeV<sup>7</sup>. For maximum flare-detection sensitivity, we select only events within a relatively small spatial region of  $1^\circ$ , this is consistent with the selection choice of events for a pulse-detection sensitivity maximization<sup>8</sup>. Note that the 68% containment angle for events of 1 GeV is about  $0.8^\circ$  for the Reprocessed Fermi-LAT data, while the 95% containment angle is about  $2^\circ$ . Note that the selection of AGNs which have no neighboring 2FGL sources within  $2^\circ$  for the study allows us to significantly suppress the effect of neighboring sources on the detection of AGN flares, since less than 5% of photons above 1 GeV from a neighboring source at a distance of  $2^\circ$  can contribute to the region with a radius of  $1^\circ$  around a source from our sample.

To perform a search for AGN flares, we began by binning events in equal exposure intervals which contain an average number of 5 photons. Note that the equal exposure intervals do not directly correspond to equal time intervals<sup>9</sup> and, therefore, we computed equal exposure intervals. Our choice of the equal exposure intervals containing 5 photons on average allows us to study AGN flares in the Poisson regime. Using the Fermi Science Tools, we calculated the exposure for each of the 394 AGNs. The calculated exposure values are in the range of  $(155 - 229) \times 10^9$  cm<sup>2</sup>s. The

<sup>4</sup> <http://heasarc.gsfc.nasa.gov/FTP/fermi/data/lat/weekly/photon/>

<sup>5</sup> [http://www.slac.stanford.edu/exp/glast/groups/canda/lat\\_Performance.htm](http://www.slac.stanford.edu/exp/glast/groups/canda/lat_Performance.htm)

<sup>6</sup> <http://fermi.gsfc.nasa.gov/ssc/data/analysis/software/v9r32p5.html>

<sup>7</sup> We use the energy threshold of 1 GeV for the selection of flares to increase photon statistics. After the selection process of flares, we will employ tight energy bands at higher energies to avoid the systematic uncertainty caused by the presence of AGNs with different spectra and by the steep energy dependence of the PSF below  $\simeq 5$  GeV.

<sup>8</sup> [http://fermi.gsfc.nasa.gov/ssc/data/analysis/scitools/pulsar\\_analysis\\_tutorial.html#extractData](http://fermi.gsfc.nasa.gov/ssc/data/analysis/scitools/pulsar_analysis_tutorial.html#extractData)

<sup>9</sup> [http://fermi.gsfc.nasa.gov/ssc/data/analysis/LAT\\_caveats\\_temporal.html](http://fermi.gsfc.nasa.gov/ssc/data/analysis/LAT_caveats_temporal.html)

mean exposure per AGN is  $171 \times 10^9 \text{ cm}^2\text{s}$  and the standard deviation is  $15 \times 10^9 \text{ cm}^2\text{s}$ . The exposure intervals containing 5 photons are in the range of  $(0.4 - 3.0) \times 10^8 \text{ cm}^2\text{s}$  with a mean of  $2.0 \times 10^8 \text{ cm}^2\text{s}$  and standard deviation of  $0.5 \times 10^8 \text{ cm}^2\text{s}$ . The mean exposure interval roughly corresponds to 2 days of *Fermi*-LAT observations.

To define an AGN flare in a statistical way, we calculate the probability of an observed number of photons in each equal exposure interval from the Poisson distribution with the mean number of photons. Furthermore, we multiply each of these probabilities by a total number of equal exposure intervals and then by 22, and compare the computed quantities with a value of 1. If the computed quantity is less than 1, we record a flare occurrence in the corresponding exposure interval. Note that the multiplications performed here guarantee that only  $\approx 5\%$  of identical sources with the same average number of photons contain such an excess of photons within one of the exposure intervals. Note that the threshold value of  $\approx 5\%$  is chosen to guarantee that most of the computed flaring intervals corresponds to the rate of photons that rarely occurs in the Poisson regime and to make our selection of flaring intervals sufficiently clean. When an AGN flare is detected, we remove this exposure interval from the data set, re-calculate the average number of photons, and repeat the procedure described above to search for the next AGN flare. Finally, we record the start and end times for all the detected flares for each AGN from our sample. The total number of the computed flaring intervals is 965, only  $\approx 2\%$  of which are expected to be due to statistical deviations in the Poisson process.

For the analysis of spatial distributions of photons for flares and for quiescent states, we bin photons in three energy bands, namely, 4.5-6 GeV, 6-10 GeV, and  $>10$  GeV. The selection of the highest energy band,  $E > 10$  GeV, is motivated by the fact that multiple scattering (see Atwood et al. 2009) is unimportant above 10 GeV and the accuracy of the directional reconstruction of photon events detected by *Fermi*-LAT is limited by the ratio of the silicon-strip pitch to silicon-layer spacing, whereas the first two energy bands are selected as tight as possible to reduce the systematic error caused by differences in the spectra of AGNs, yet still have enough photons for a meaningful statistical analysis. The 95% containment angles for photon events from a point-like source belonging to these energy bands are about  $0.5^\circ$ <sup>10</sup>. For each energy band, we bin photons in annular bins with radii of  $0^\circ < r < 0^\circ.21$ ,  $0^\circ.21 < r < 0^\circ.30$ ,  $0^\circ.30 < r < 0^\circ.42$ ,  $0^\circ.42 < r < 0^\circ.52$ ,  $0^\circ.52 < r < 0^\circ.60$ , and  $1^\circ.0 < r < 1^\circ.3$ . Note the first two annular bins have a surface area twice smaller than those of the 3rd, 4th, and 5th bins<sup>11</sup>. This selection is motivated by the fact that the statistics for the first two bins is sufficient to perform the analysis. We do not divide the 1st annular bin into tighter annular bins in order to eliminate the effect caused by the uncertainties in the determination of AGN positions on the  $\gamma$ -ray sky in the

2FGL catalog. The outer annular bin is selected for an estimation of the rate of background photons and has a surface area which is  $\approx 7.7$  times larger than that of the 3rd, 4th, and 5th bins.

In Sect. 3.2, we demonstrate an application of the temporal analysis based on the separation of photon events recorded during AGN flares from those during quiescent states for a search for pair halos. Pair halos around AGNs are expected to possibly reveal themselves as an extended emission component in addition to a point source emission from AGNs. Note that the size of the extended component should be redshift-dependent. This dependence on a source redshift is caused by 1) a redshift-dependent deflection angle of secondary electrons and positrons in extragalactic magnetic fields (see Eqs. 30 and 31 from Neronov & Semikoz (2009)), and 2) the geometry of propagation of cascade  $\gamma$  rays from the source to the observer (see Eq. 33 from Neronov & Semikoz (2009)). Note that the motion of the secondary electron-positron pairs is determined by the value of the correlation length of the extragalactic magnetic field. Thus, if the correlation length,  $\lambda_B$ , is much less than electron cooling distance  $D_e$ , within which secondary electrons/positrons lose their energy via IC scattering of the CMB photons, deflections of secondary electrons/positrons are described as diffusion in angle. In the opposite case, motion of secondary electrons and positrons at the length scale of  $D_e$  can be approximated by their motion in a homogeneous magnetic field. The redshift dependencies are different for both these cases of motion. Apart from the redshift dependence due to motion of secondary electrons and positrons, geometry of  $\gamma$ -ray propagation introduces another redshift dependent factor which is determined by the ratio of a mean free path of primary TeV  $\gamma$  rays propagating through the EBL to a distance from the source. Below we perform two different analyses to search for a pair halo component to compromise between the number of detected photon events and the tightness of redshift bins.

In Sect. 3.1, we start with a study of the spatial distributions of photons recorded during AGN flare and quiescent states. In Sect. 3.2, we will bin the AGNs from our sample in several redshift bands to search for pair halos in each of these selected redshift-dependent samples. Finally, in Sect. 4.1, we will perform a search for pair halos for individual strong AGNs included in our sample.

### 3.1 AGN flare and quiescent states

To extract the approximate PSF on the basis of photons recorded during AGN flares, we only use photons from AGNs that show the presence of flaring activity. Our final sample then contains 158 AGNs including 56 BL Lac type blazars of which 5 are definite identifications, 92 flat spectrum radio quasars of which 6 are definite identifications, 7 active galaxies of uncertain type, and 3 non-blazar AGNs of which 1 is a definite identification. The ten brightest AGNs from our final sample, corresponding to the 2FGL catalog, are PKS 1510-089, PKS 0537-441, 4C +21.35, Markarian 421, 3C 279, AO 0235+164, B2 1520+31, 3C 273, PKS 1424+240, and PKS 0447-439. *Fermi*-LAT observations revealed the flaring activity of PKS 1510-089 (Abdo et al. 2010a), 4C +21.35 (Ackermann et al. 2014), 3C 279 (Ciprini & Chaty 2008), B2 1520+31 (Cutini & Hays 2009; Sanchez 2010), 3C

<sup>10</sup> [http://www.slac.stanford.edu/exp/glast/groups/canda/archive/p7rep\\_v15/lat\\_Performance\\_files/cPsfEnergy\\_P7REP\\_SOURCE\\_V15.pdf](http://www.slac.stanford.edu/exp/glast/groups/canda/archive/p7rep_v15/lat_Performance_files/cPsfEnergy_P7REP_SOURCE_V15.pdf)

<sup>11</sup> the surface areas of the 1st and 2nd annuli are chosen to be equal and the surface areas of the 3rd, 4th, and 5th annuli are chosen to be equal. For the sake of brevity, in the paper we write the approximate values of the bin angular size.

273 (Abdo et al. 2010c), and PKS 1424+240 (Donato 2010; Szostek 2011).

In this Section, we obtain the spatial distribution of  $\gamma$  rays recorded during AGN flares. This distribution should approximate the PSF well (see Sect. 4.2). We also compare this spatial distribution with that obtained from observations of a large sample of AGNs during their quiescent states. A large sample of AGNs contain  $\gamma$ -ray sources at different redshifts (see Sect. 3.2). Since the size of pair halos strongly depends on redshift, the contribution of pair halos with very different sizes to  $\gamma$ -ray emission of a particular size is expected to be small. Below the comparison between these distributions will establish that these spatial distributions are similar, and further, we will proceed by sorting AGNs in redshift bins in Sect. 3.2 to maximise the relative contribution from pair halos to the  $\gamma$ -ray signal.

We stacked the photon events separately for flares and for quiescent states for each selected energy band and each selected annular bin, using our sample of the selected AGNs and the computed flaring and quiescent states. The distribution of photons coming from AGN flaring states is computed for our sample of 158 AGNs showing flaring activity, while the distribution of photons coming from AGN quiescent states is computed for the sample of the 394 selected AGNs (see Sect.3). The stacked distributions of photons in annular bins for flares and for quiescent states are presented in Table A1.

We used the stacked distributions of photons in annular bins for flares and for quiescent states to derive the ratio of the number of photons coming from AGNs and detected during quiescent states to the number of photons coming from AGNs and detected during flares,  $R_{Q/F}$ . We performed this procedure for each annular bin and each selected energy band separately. The statistical error taken was the square root of the count number. To subtract background photons, we used the number of photons within the outer annular bin,  $1^\circ < r < 1.3^\circ$ , which is  $\approx 7.7$  ( $\approx 15.4$ ) times larger than the 3rd, 4th, and 5th annular bins (the 1st and 2nd annular bins), respectively. The errors in the determination of background photon numbers were taken into account. The calculated numbers of photons in annular bins for flares and for quiescent states for each selected energy band after subtraction of a background are shown in Table A2. Note that the calculated number of photons for AGN flares provides us with similar statistics as provided by the Crab pulsar and accumulated by *Fermi*-LAT during 3.5 years (see Sect. 5.1). The calculated ratios,  $R_{Q/F}$ , and statistical errors are shown in Table A3. The calculated ratios are within the error bars for each energy bin. We also calculated the weighted mean of these ratios in the annular bin of  $0^\circ.21 < r < 0^\circ.6$  for each energy band and the variance of the mean. The weighted mean of the ratios agrees with the ratio computed for the first annular bin (this bin contains the highest number of photons amongst all the bins, and therefore, provides the smallest statistical error).

Note that the ratio of the number of photons from AGNs to that from a background is much higher for flares than for quiescent states and that the ratio of the number of photons from AGNs to that from a pair halo component is much higher for flares than for quiescent states. These conclusions about the ratios are equivalent to the suggestion that the flux from an AGN (from our sample) during its

flaring state is higher than that during its quiescent state. We found that 34 bright flaring AGNs from our sample during their flaring states gives 80% of  $\gamma$  rays above 4.5 GeV recorded during the flaring states of all 158 AGNs in the sample. To establish that the average flux during the flaring state of an AGN is higher than that during the quiescent state, we computed the ratio of the average flux recorded during flares to that during the quiescent state for each of these 34 bright flaring AGNs. We found that these ratios exceed 5 for all these 34 AGNs, while the ratios exceed 10 for 18 of these 34 AGNs. The ratio of the mean flux recorded during flaring states to that recorded during quiescent states for other flaring AGNs of our sample is  $\approx 5$ <sup>12</sup>. The fact that it is more promising to search for a pair halo during quiescent states than to search for a pair halo during flaring states was first emphasized by Aharonian et al. (1994) and was used by Barbiellini et al. (2014) in their analysis of 3C 279.

We also noted that the ratio of the number of photons coming from AGNs and detected during quiescent states to that detected during flares is higher for the energy band of  $E > 10$  GeV compared with those for the energy bands of  $4.5 \text{ GeV} < E < 6 \text{ GeV}$  and  $6 \text{ GeV} < E < 10 \text{ GeV}$ . A probable explanation is the presence of the selection bias because the sample of 394 sources contains 185 BL Lac type blazars and 146 FSRQs, while the sample of 158 sources contains 56 BL Lac type blazars and 92 FSRQs.

We also repeated our analysis and computed the ratio of the number of photons coming from AGNs and detected during quiescent states to the number of photons coming from AGNs and detected during flares by using only the sample of the 158 AGNs showing flaring activity (this guarantees the same ratio of the numbers of BL Lac type blazars to FSRQs for which flares and quiescent states are recorded). This is useful to suppress a possible selection effect due to considering different AGN samples for flaring and quiescent states. These ratios are shown in Table 1. The calculated ratios are also within the error bars for each energy bin. The ratios shown for the first annular bin are statistically significantly different between the energy band,  $> 10\text{GeV}$ , and the other two energy bands. However, a detailed study of this question is beyond of the scope of our paper. Note that the ratio computed for the numbers of background photons (i.e. those from the outer annuli) recorded during AGN flares and quiescent states does reveal any change from one energy band to another. This indicates that the changing of the ratio with energy as described is related to the AGN themselves rather than to any background variation in time.

<sup>12</sup> Note that this does not mean that the factor of 5 difference in “flaring” versus “quiescent” states is a result of the selection of the mean number of photons of 5 in each exposure interval, i.e. the mean flux ratio between flaring and quiescent states would not become 10, if the mean number of photons of 10 in each exposure interval is selected. Thus, for example if a flare is short and lies within one exposure interval then the flaring-to-quiescent flux ratio will be higher for a smaller mean number of photons within one exposure interval. On the other hand, if a flare is long, for example with the duration half a total exposure then the flaring-to-quiescent flux ratio will not depend on the mean number of photons within one exposure interval.

**Table 1.** The ratio of the number of photons coming from 158 AGNs and detected during quiescent states to the number of photons coming from AGNs and detected during flares

Annular bin	Energy bands		
	4.5 – 6 GeV	6 – 10 GeV	> 10 GeV
$0^\circ < r < 0^\circ.21$	$3.2 \pm 0.2$	$3.38 \pm 0.15$	$4.7 \pm 0.2$
$0^\circ.21 < r < 0^\circ.3$	$2.9 \pm 0.3$	$2.9 \pm 0.3$	$5.2 \pm 0.7$
$0^\circ.3 < r < 0^\circ.42$	$2.8 \pm 0.3$	$3.7 \pm 0.5$	$4.9 \pm 0.9$
$0^\circ.42 < r < 0^\circ.52$	$4.3 \pm 0.9$	$3.1 \pm 0.7$	$4.7 \pm 1.1$
$0^\circ.52 < r < 0^\circ.6$	$3.3 \pm 1.0$	$4.5 \pm 1.4$	$2.5 \pm 1.3$

### 3.2 Search for pair halos around AGNs within several redshift intervals

The sizes of pair halos depend on the source redshifts and, therefore, to search for pair halos around AGNs the redshifts should be taken into account. Below, we present the temporal analysis for samples of AGNs with known redshifts belonging to several redshift intervals. Using the second catalog of AGNs detected by *Fermi*-LAT (Ackermann et al. 2011) we select only the AGNs with known redshifts from our sample of 394 AGNs. Since the number of photon events coming during AGN flares is much smaller ( $\sim 5$  times) than that that coming during quiescent states (see Table A2), we will use all 158 AGNs showing  $\gamma$ -ray flaring activity to approximate the PSF using flares of AGNs. To have a higher number of photons during AGN quiescent states, we select all AGNs with known redshifts from our sample of 394 AGNs. We sort AGNs in redshift intervals only for quiescent states.

To perform the analysis within several redshift intervals, the redshift intervals should be as tight as possible to expect a similar angular extension of pair-halos within each redshift interval and should be as broad as possible to increase the number of photon events from AGNs within similar redshifts. In this paper, we sort the AGNs with known redshifts belonging to our sample into four redshift intervals,  $z < 0.2$ ,  $0.2 < z < 0.6$ ,  $0.6 < z < 1.3$ , and  $1.3 < z$ . The numbers of AGNs in these redshift intervals are 34, 60, 83, and 57, respectively, i.e., 234 AGNs with known redshifts in total. Note that these redshift intervals are tighter than those chosen by Ando & Kusenko (2010) which were  $z < 0.5$  and  $0.5 < z$ . We introduce two redshift intervals to gather nearby AGNs ( $z < 0.2$ ) in one of these two intervals and very distant AGNs ( $z > 1.3$ ) in the other interval. Since the size of extended emission from pair halos steeply decreases with distance and is proportional to the strength of extragalactic magnetic field (see, e.g., Neronov & Semikoz 2009), the introduction of these two redshift intervals allows us to cover the cases of a lower and a higher strength of extragalactic magnetic field. We estimated the strength of extragalactic magnetic field which can be tested using the present analysis by assuming that the angular extension of pair halos within each redshift interval is  $0.3^\circ$  and that the correlation length,  $\lambda_B$ , is much less than the electron cooling distance  $D_e$ . Putting the values of the redshift and angular extension in Eq. 35 of (Neronov & Semikoz 2009), we found that the values of strength of extragalactic magnetic field which can be tested by using this analysis,  $B \times (\lambda_0/1\text{kpc})^{1/2}$ , are about  $10^{-15}$ ,  $10^{-14}$ ,  $5 \times 10^{-14}$ , and  $10^{-13}$  gauss for the redshift intervals of  $z < 0.2$ ,  $0.2 < z < 0.6$ ,  $0.6 < z < 1.3$ , and

$1.3 < z$ , respectively<sup>13</sup>. The stacked distributions of photons in annular bins for quiescent states of AGNs within the four redshift intervals are presented in Table A4.

To justify the usage of the front-converting and back-converting events together for the increase of statistics, we compute the ratio of the number of front-converting events to that of back-converting events (the front-to-back ratio) recorded during quiescent AGN states for each redshift interval and recorded during AGN flares, respectively. We compute the front-to-back ratios for each energy band individually and compare these ratios computed for quiescent states and flares. The front-to-back ratios for flares are  $1.50 \pm 0.10$  for the 4.5-6 GeV band,  $1.42 \pm 0.09$  for the 6-10 GeV band, and  $1.54 \pm 0.11$  for the  $> 10$  GeV band, while the central values of the front-to-back ratios for quiescent states are in the range of  $\approx 1.30 - 1.45$  for each of the redshift intervals and each of the energy bands. We checked that the front-to-back ratios for quiescent states lie within the  $2\sigma$  error bars around the central values for the front-to-back ratio computed for flares (i.e., are consistent with the  $2\sigma$  confidence level). Since the PSF for front-converting events are tighter than that for back-converting events, the effect of an excess of the front-to-back ratio for flares compared with that for quiescent states could mimic the presence of a pair halo. We do not detect this effect (neither do we detect pair halos) using the present data and conclude that this effect is subdominant. Although this effect does not produce an observable spurious extension of the sources during their quiescent states, this effect can still produce a systematic bias on the upper limit on pair halos derived in the paper. Since the existing data does not show any significant difference in the front-to-back ratio for flares and for quiescent states, we leave this question for studying in the future when higher statistics will be accumulated.

To compare the spatial distributions of photons detected during quiescent states of AGNs within the given redshift interval with that of photons detected during the flares of AGNs from our final sample of 158 AGNs, we divide these numbers by each other after subtraction of a background. The ratios of these numbers of photons for each annular bin and each energy band are shown in Table 2. Note that background rates and statistical errors were estimated in the same way as the analysis of photons from AGNs belonging to our final sample presented above. If the relative error on the ratio is high, we do not list such a value in this Table. The calculated ratios are in general within the error bars for each energy bin and each redshift interval. Therefore, no evidence for a pair halo component is found in any of the selected redshift intervals.

#### 3.2.1 Upper limits for the fraction of $\gamma$ rays attributable to a pair halo component

To set the upper limits for the fraction of  $\gamma$  rays attributable to a pair halo component, we should make an assumption about the spatial profile of a pair halo (e.g., see

<sup>13</sup> To obtain the magnetic field strength which can be tested by using AGNs in the redshift interval of  $z < 0.2$ , we assume that the strongest sources, Mkn 421 and Mkn 501, give the strongest contribution to pair halo emission.

**Table 2.** The ratio of the number of photons detected during quiescent states of AGNs within the given redshift interval with that of photons detected during the flares of AGNs from our entire sample.

Redshift	Annular bin	Energy bands		
		4.5 – 6 GeV	6 – 10 GeV	> 10 GeV
$z < 0.2$	$0^\circ < r < 0^\circ.21$	$0.85 \pm 0.05$	$1.07 \pm 0.06$	$2.15 \pm 0.11$
$z < 0.2$	$0^\circ.21 < r < 0^\circ.3$	$0.82 \pm 0.09$	$0.89 \pm 0.11$	$2.28 \pm 0.35$
$z < 0.2$	$0^\circ.3 < r < 0^\circ.42$	$0.66 \pm 0.10$	$0.94 \pm 0.15$	$2.35 \pm 0.43$
$z < 0.2$	$0^\circ.42 < r < 0^\circ.52$	$0.99 \pm 0.27$	$1.03 \pm 0.28$	$2.03 \pm 0.53$
$z < 0.2$	$0^\circ.52 < r < 0^\circ.6$	–	–	$1.02 \pm 0.65$
$0.2 < z < 0.6$	$0^\circ < r < 0^\circ.21$	$0.90 \pm 0.06$	$0.93 \pm 0.05$	$1.36 \pm 0.07$
$0.2 < z < 0.6$	$0^\circ.21 < r < 0^\circ.3$	$0.81 \pm 0.13$	$0.74 \pm 0.09$	$1.44 \pm 0.22$
$0.2 < z < 0.6$	$0^\circ.3 < r < 0^\circ.42$	$0.75 \pm 0.10$	$1.16 \pm 0.16$	$1.29 \pm 0.24$
$0.2 < z < 0.6$	$0^\circ.42 < r < 0^\circ.52$	$1.51 \pm 0.30$	$1.23 \pm 0.25$	$1.53 \pm 0.36$
$0.2 < z < 0.6$	$0^\circ.52 < r < 0^\circ.6$	$0.83 \pm 0.25$	$2.10 \pm 0.57$	$2.14 \pm 0.70$
$0.6 < z < 1.3$	$0^\circ < r < 0^\circ.21$	$1.04 \pm 0.06$	$1.07 \pm 0.06$	$1.17 \pm 0.07$
$0.6 < z < 1.3$	$0^\circ.21 < r < 0^\circ.3$	$0.95 \pm 0.11$	$1.11 \pm 0.13$	$1.30 \pm 0.23$
$0.6 < z < 1.3$	$0^\circ.3 < r < 0^\circ.42$	$0.90 \pm 0.15$	$1.02 \pm 0.20$	$1.26 \pm 0.31$
$0.6 < z < 1.3$	$0^\circ.42 < r < 0^\circ.52$	$1.39 \pm 0.40$	$0.83 \pm 0.31$	$1.08 \pm 0.43$
$0.6 < z < 1.3$	$0^\circ.52 < r < 0^\circ.6$	–	$1.50 \pm 0.72$	–
$1.3 < z$	$0^\circ < r < 0^\circ.21$	$0.58 \pm 0.04$	$0.41 \pm 0.03$	$0.43 \pm 0.03$
$1.3 < z$	$0^\circ.21 < r < 0^\circ.3$	$0.51 \pm 0.07$	$0.37 \pm 0.07$	$0.31 \pm 0.11$
$1.3 < z$	$0^\circ.3 < r < 0^\circ.42$	$0.48 \pm 0.10$	$0.58 \pm 0.13$	$0.60 \pm 0.21$
$1.3 < z$	$0^\circ.42 < r < 0^\circ.52$	$0.90 \pm 0.29$	$0.77 \pm 0.26$	–
$1.3 < z$	$0^\circ.52 < r < 0^\circ.6$	$0.63 \pm 0.40$	$0.97 \pm 0.29$	–

Ackermann et al. 2013). Note that if the pair halo profile is narrow compared with the PSF, it would be difficult to disentangle a point-like component from a pair halo. Therefore, in this analysis we assume that a pair halo is an extended component to *Fermi*-LAT with an angular size of  $\gtrsim 0.3^\circ$  (which exceeds the radius of the second annular bin). Since the signal-to-noise ratios of the  $\gamma$ -ray signal from the stacked source centered on AGNs are highest for the first and second annular bins, we will use these two annular bins to set the upper limits for the fraction of  $\gamma$  rays attributable to a pair halo component. Note that the fluxes from AGNs during episodes of  $\gamma$ -ray flares are much higher than those during quiescent states due to the definition of flares (see the beginning of Section 3) and, therefore, the contribution of a pair halo component to flare fluxes is negligible compared to that of quiescent state fluxes. Thus, we assume that the contribution to the first and second annular bins from a pair halo component are the same for quiescent AGN states and that the contribution from a pair halo component to AGN flares is negligible. First we divided the number of photons after the subtraction of a background in the first bin by that in the second bin for AGN flares and for quiescent AGN states. Second we subtracted the equal number of photons,  $x$ , from the first and second annular bins for quiescent AGN states (these photons come from a possible pair halo component). After this procedure, the ratios of the number of photons must be the same. Thus, this procedure leads to the equation for the ratios of the numbers of photons in the first and second annular bins for the energy band of 4.5-6 GeV and for the redshift interval,  $z < 0.2$ ,

$$\frac{504 - 19 \pm 22 - x}{165 - 19 \pm 13 - x} = \frac{570 \pm 24}{178 \pm 14}, \quad (1)$$

where the left-hand side of this equation is for quiescent states (see Table A4) and the right-hand side is for flares (see Table A2). The equations for the energy band of 6-10 GeV and  $>10$  GeV were obtained using the same procedure. Taking the error bars into account, we computed the 95%

upper limit for the fractions of  $\gamma$  rays from the stacked AGN sample attributable to a pair halo component in the first annular bin ( $r < 0.21^\circ$ ) for each selected redshift interval. The computed 95% upper limits are shown in the upper part of Table 3.

Note that the obtained constraints on the fraction of  $\gamma$  rays attributable to a pair halo component were derived under the assumption that a pair halo component does not contribute to the region of  $1^\circ.0 < r < 1^\circ.3$ . This region was used to estimate a background. Using the number of photons in the outer annular bin (see Table A4), we found that the fraction of  $\gamma$  rays from the stacked AGN sample attributable to a background in the first annular bin ( $r < 0^\circ.21$ ) is 2-4% for the three energy bands and for the redshift interval of  $z < 0.2$ , 4-6% for the three energy bands and for the redshift interval of  $0.2 < z < 0.6$ , 6-7% for the three energy bands and for the redshift interval of  $0.6 < z < 1.3$ , and 9-11% for the three energy bands and for the redshift interval of  $z > 1.3$ . The assumption that a pair halo component does not contribute to the region of  $1^\circ.0 < r < 1^\circ.3$  can be weakened. For this purpose, we modified the procedure described above. First we divided the number of photons without the subtraction of a background (see Table A2) in the first bin by that in the second bin for AGN flares and for quiescent AGN states. Second we subtracted the equal number of photons,  $x$ , from the first and second annular bins for quiescent AGN states (these photons come from a possible pair halo component + a background). Note that a background contributes the same number of photons in the first and second annular bins, because their surface areas are the same. Thus, this procedure leads to the equation for the ratios of the numbers of photons in the first and second annular bins for the energy band of 4.5-6 GeV and for the redshift interval,  $z < 0.2$ ,

$$\frac{504 \pm 22 - x}{165 \pm 13 - x} = \frac{574 \pm 24}{182 \pm 14}, \quad (2)$$

where the left-hand side of this equation is for quiescent

**Table 3.** The 95% upper limits for the fractions of  $\gamma$  rays from the stacked AGN sample attributable to a pair halo component in the first annular bin ( $r < 0.21^\circ$ ) for each selected redshift interval.

Redshift	background	Energy bands		
		4.5 – 6 GeV	6 – 10 GeV	> 10 GeV
$z < 0.2$	subtracted	12%	7%	6%
$0.2 < z < 0.6$	subtracted	11%	7%	10%
$0.6 < z < 1.3$	subtracted	11%	9%	6%
$1.3 < z$	subtracted	15%	11%	7%
$z < 0.2$	included	13%	7%	6%
$0.2 < z < 0.6$	included	11%	8%	10%
$0.6 < z < 1.3$	included	15%	12%	12%
$1.3 < z$	included	20%	17%	15%

states (see Table A4) and the right-hand side is for flares (see Table A1). We compute the 95% upper limits for the fraction of  $\gamma$  rays from the stacked AGN sample attributable to a pair halo component + a background in the first annular bin ( $r < 0.21^\circ$ ). The computed 95% upper limits are shown in the bottom part of Table 3.

### 3.2.2 Validation with a likelihood analysis

To strengthen the results obtained above, we use a likelihood analysis. This analysis permits us to search for a pair halo component around AGNs in the LAT telescope data and to set upper limits on the fraction of photons attributable to this component. Likelihood is the joint probability of the observed data given the hypothesis and quantifies the relative extent to which the data supports a statistical hypothesis. Below we consider the null hypothesis which implements that gamma-ray emission from AGNs comes from compact sources which are point-like gamma-ray sources for the LAT telescope. As the alternative hypothesis, we consider that gamma-ray emission from AGNs comes from both the compact sources and extended pair halo component. A likelihood function (often the likelihood) is a function of the parameters of a statistical model (in our case, these parameters are the normalisations of a point-like component and of a pair halo component).

We use the same 234 AGNs with known redshifts which were used above in this Section. As done above, we sort these AGNs into four redshift intervals,  $z < 0.2$ ,  $0.2 < z < 0.6$ ,  $0.6 < z < 1.3$ , and  $1.3 < z$  and bin photons in three energy bands, namely, 4.5-6 GeV, 6-10 GeV, and  $> 10$  GeV. To perform a likelihood analysis, we sort photons in six annuli,  $0 < r < 0.05^\circ$ ,  $0.05 < r < 0.1^\circ$ ,  $0.1 < r < 0.15^\circ$ ,  $0.15 < r < 0.20^\circ$ ,  $0.20 < r < 0.25^\circ$ , and  $0.25 < r < 0.30^\circ$ . We have performed maximum likelihood analysis assuming that, in addition to the central point sources and diffuse backgrounds, there is a pair halo component. We fit the histogram of photon counts as a function of  $\theta^2$  by minimising

$$\chi^2 = \sum_i \frac{(N_i - N_{\text{model},i})^2}{N_i}, \quad (3)$$

and

$$N_{\text{model},i} = N_{\text{psf}} P_{\text{psf}}(\theta_i^2) + N_{\text{halo}} P_{\text{halo}}(\theta_i^2) + N_{\text{bg},i}, \quad (4)$$

where  $N_{\text{psf}}$  and  $N_{\text{halo}}$  are free parameters of the alternative model (see also Ando & Kusenko (2010)). As for the null model  $N_{\text{psf}}$  is a free parameter and the parameter  $N_{\text{halo}}$

equals zero by definition. The index  $i$  refers to the  $i$ -th annular bin,  $N_i$  is the total number of events in the annular bin recorded during flaring states.  $P_{\text{psf}}$  is the normalised PSF and  $N_{\text{bg},i}$  is the number of events due to diffuse backgrounds. To estimate the rate of background photons, we use the outer (large) annular bin,  $1.0 < r < 1.3^\circ$ , and compute the number of background photons in each of six annular bins by using surface area scales. In this analysis we assume that a pair halo, described as  $P_{\text{halo}}$ , is an extended component to Fermi-LAT with an angular size of  $\gtrsim 0.3^\circ$  and its contribution to each of the six annular bins is proportional to the surface areas of these annular bins, respectively. The normalised PSF is taken from the distribution of photons recorded during AGN flares.

From the result of the  $\chi^2$  minimisation, we found that the minimised  $\chi^2$  values agree with the expected values, i.e. the computed  $\chi^2$  are typically in the range of (d.o.f.  $-\sqrt{2\text{d.o.f.}}$ , d.o.f.  $+\sqrt{2\text{d.o.f.}}$ ), where d.o.f. is the number of degrees of freedom. This means that the fits describe the observed data rather well. The only exception is with  $\chi^2 \approx 20$ , which occurs for nearby AGNs,  $z < 0.2$ , and for the highest energy band,  $E > 10$  GeV. Note that there is a strong contribution of the source, Mkn 421, in the 1st redshift interval at high energies,  $E > 10$  GeV for quiescent states. Mkn 421 is a very hard spectrum gamma-ray source with a photon index of  $\approx 1.77$  and its semiminor and semimajor axes at 68% confidence are of  $0.0067^\circ$  as derived in Nolan et al. (2012). Semiminor and semimajor axes of many 2FGL sources are derived with one order of magnitude higher uncertainties than those for Mkn 421 in the 2FGL catalog Nolan et al. (2012). We noted that the discrepancy between the observation and model is particularly strong in the annular bin,  $r < 0.05^\circ$ , for the redshift interval  $z < 0.2$  and for the highest energy band,  $E > 10$  GeV. If we exclude photons from Mkn 421, then the minimised  $\chi^2$  value is 7.5 and is consistent with the expected one. In the limit of a large number of counts in each bin, the likelihood is given by  $\mathcal{L} = \exp(-\chi^2/2)$ , so that minimising  $\chi^2$  is equivalent to maximising the likelihood,  $\mathcal{L}$ . We found that the inclusion of a pair halo component in the model does not improve the likelihood value sufficiently to establish the presence of this pair halo component in the data. Therefore, we derived the one-sided 95 per cent upper limit on the fraction of photons attributable to a pair halo component by fitting the normalisation of this component, for which we increase its normalisation until the maximum likelihood decreases by 2.71/2 in logarithm. The computed upper limits are between 2% and 6% depending on energy band and



redshift interval. These upper limits are stronger than those obtained before. Note that the model for a point-like source used in the likelihood analysis is considered to be precisely established, however the number of photons recorded during flaring states is close to those numbers of photons recorded during quiescent states for each of these redshift intervals. The expression, such as Eq.1, leads to more conservative upper limits on the fraction of photons attributable to a pair halo component, since it takes the error bars assigned to the model into account. If the point-like source model is considered well established, then the error bars shown in Table 3 would decrease by a factor of  $\approx 1.5$ ).

We also checked if the computations presented above are reproducible by maximising the Poisson log-likelihood function,  $l = \ln \mathcal{L}$ , where

$$l = \sum_i N_i \ln N_{\text{model},i} - \sum_i N_{\text{model},i}. \quad (5)$$

Maximising the Poisson log-likelihood function, we found that the best-fit normalisations of the point-like component and the upper limits on the pair halo component agree well with those derived by using the  $\chi^2$  minimisation.

#### 4 METHOD TO RECONSTRUCT THE FERMI-LAT PSF

In this Section, we perform a temporal analysis of each of the five brightest  $\gamma$ -ray AGNs from our sample in order to search for pair halos around each of these sources. Further we reconstruct the *Fermi*-LAT PSF which is not affected by a pair halo component.

As was mentioned above, the contribution of a pair halo component to the total AGN  $\gamma$ -ray emission is much smaller for flares than that for quiescent states. Therefore, the spatial distribution of photons coming during AGN flares can be used as a proxy of the PSF.

The spatial distribution of photons coming during quiescent AGN states,  $D_Q(x)$ , for each energy band and each source can be written as

$$D_Q(x) = \alpha_Q \text{PSF}(x) + H_Q(x) + B_Q(x), \quad (6)$$

where the first, second, and third terms are the contributions of a point source, a pair halo, and a background, respectively, and  $x$  is the label for annular bins,  $\alpha_Q$  is the normalisation of a point source flux. Note that the PSF component is not affected by a pair halo component. Similarly the spatial distribution of photons coming during AGN flares,  $D_F(x)$ , can be written as

$$D_F(x) = \alpha_F \text{PSF}(x) + H_F(x) + B_F(x). \quad (7)$$

The pair halo and background fluxes are time-invariant and, therefore,

$$\frac{H_F(x) + B_F(x)}{H_Q(x) + B_Q(x)} = \frac{N_F}{N_Q}, \quad (8)$$

where  $N_Q$  and  $N_F$  are the total number of equal exposure intervals for quiescent states and for flares, respectively, for the given AGN. Multiplying Eqs. 6 and 7 by  $N_F$  and  $N_Q$ , respectively, and subtracting one equation from the other, we find

$$\text{PSF}(x) = \frac{D_F(x)N_Q - D_Q(x)N_F}{\alpha_Q N_F - \alpha_F N_Q}. \quad (9)$$

Note that the ratio of the values of the point spread function for two annular bins depends only on the values of  $D_F(x)N_Q - D_Q(x)N_F$  for these annular bins. This fact can be used to reconstruct the PSF by computing the ratios of the PSF values for different annular bins.

#### 4.1 Analysis of individual sources

To outline the method of the PSF reconstruction, below we calculate the ratio,  $R$ , of the values of the point spread function for the two annular bins of  $0 < r < 0^\circ.21$  and  $0^\circ.21 < r < 0^\circ.42$ . Note that the later annular bin corresponds to the sum of the second and third annular bins from Table A2. For this study, we selected the five brightest sources from our final sample, namely 4C +21.35, 3C 279, PKS 1510-08, PKS 0537-441, and Mkn 421. We calculate the ratio,  $R$ , for each of these sources and the weighted mean of these ratios. For an illustration, we selected photons in the energy band of 4.5-6 GeV and photons in the energy band of 6-10 GeV. The observed numbers of photons in the two annular bins of  $0 < r < 0^\circ.21$  and  $0^\circ.21 < r < 0^\circ.42$  for flares and for quiescent states for the five brightest sources are shown in Table A5. Using Eq. 9 and Table A5, we calculated the ratios of the values of the point spread function for these two annular bins,  $R$ , for the five brightest sources. The calculated ratios are shown in Table 4. The weighted mean of the ratios for these five sources is  $\bar{R} = 1.7 \pm 0.3$  for the energy band of 4.5-6 GeV and is  $\bar{R} = 2.7 \pm 0.4$  for the energy band of 6-10 GeV. We compared the calculated weighted mean of the ratios for these five sources for the energy band of 4.5-6 GeV,  $\bar{R} = 1.7 \pm 0.3$ , with the ratio of the numbers of photons in these two annular bins for flares and for quiescent states (see Table A2). The ratios of the numbers of photons in these two annular bins coming during flares and quiescent states are  $R_F = 1.9 \pm 0.1$  and  $R_Q = 2.2 \pm 0.1$ , respectively. All these three ratios ( $\bar{R}$ ,  $R_F$ , and  $R_Q$ ) agree within the error bars. Note that the value of  $\bar{R}$  is close to that of  $R_F$  as was expected. We also compared the calculated weighted mean of the ratios for these five sources for the energy band of 6-10 GeV,  $\bar{R} = 2.7 \pm 0.4$ , with the ratio of the numbers of photons in these two annular bins for flares and for quiescent states,  $R_F = 2.7 \pm 0.2$  and  $R_Q = 2.8 \pm 0.1$ , respectively. These three values ( $\bar{R}$ ,  $R_F$ , and  $R_Q$ ) agree within the error bars for the energy band of 6-10 GeV. Therefore, no evidence for a pair halo is found by means of these comparisons.

We also obtained the constraints on the fraction of  $\gamma$  rays attributable to a pair halo component for each of the five brightest AGNs. We divided the number of photons without the subtraction of a background (see Table A5) in the first bin by that in the second bin for quiescent AGN states and for AGN flares. Then we subtracted the number of photons,  $x$ , from the first annular bin and subtracted the number of photons,  $3x$ , from the second annular bin<sup>14</sup> for quiescent AGN states (these photons come from a possible pair halo component + a background). To improve the constraints we used our final sample of 158 AGNs to compute the number of photons during AGN flares. We found

<sup>14</sup> The factor of 3 is due to a larger surface area of the second annular bin compared with that of the first annular bin.

**Table 4.** The ratios,  $R$ , of the values of the point spread function for the first two annular bins and for the energy bands of 4.5-6 GeV and 6-10 GeV.

Source name	$R$ for 4.5-6 GeV	$R$ for 6-10 GeV
4C +21.35	$1.5 \pm 0.4$	$2.9 \pm 0.8$
3C 279	$1.5 \pm 0.6$	$1.9 \pm 1.0$
PKS 1510-08	$2.7 \pm 0.8$	$2.4 \pm 0.7$
PKS 0537-441	$2.2 \pm 0.8$	$3.8 \pm 1.2$
Mkn 421	$2.6 \pm 1.5$	$4.4 \pm 2.1$
weighted mean	$1.7 \pm 0.3$	$2.7 \pm 0.4$

that the 95% upper limit for the fraction of  $\gamma$  rays from the stacked AGN sample attributable to a pair halo component + a background in the first annular bin ( $r < 0.21^\circ$ ) equals 20% for the energy band of 4.5-6 GeV and 7% for the energy band of 6-10 GeV for 4C+21.35. For the other four selected AGNs these ratios for the energy bands of 4.5-6 GeV and 6-10 GeV are 10% and 19% for 3C 279, 13% and 7% for PKS 1510-08, 7% and 5% for PKS 0537-441, and 12% and 4% for Mkn 421. Note that as a proxy of the PSF for the computation of the upper limits on the fraction of  $\gamma$  rays attributable to a pair halo component, we used the spatial distribution of photons coming from AGNs during their flares.

## 4.2 Reconstruction of the Fermi-LAT PSF

The onboard data obtained by the LAT instrument can be used to derive its instrument response functions, such as the PSF. To perform a reconstruction of the PSF, one needs to select an astrophysical  $\gamma$ -ray source which is point-like for the instrument. One class of  $\gamma$ -ray sources used for the PSF reconstruction is pulsar; another class used for this is AGN. However, the presence of pair halos around AGNs limits the application of AGNs for the PSF reconstruction. In this Section, we demonstrate how to reconstruct the *Fermi*-LAT PSF that is not affected by a pair halo component by stacking 158 flaring AGNs of our sample.

We take each of the 158 flaring sources of our sample and derive the angular distribution of  $\gamma$  rays for each source for both flaring and quiescent states. Then we compute the value of  $D_F(x)N_Q - D_Q(x)N_F$  for each source and for each annular bin. This gives the “pure” PSF profile, free of the possible extended pair-halo signal. Then we stack the PSF profile obtained in this way on a source-by-source basis for all the 158 sources to increase the signal statistics. For the sake of convenience, we choose the normalisation of the obtained profiles for each of the three energy bands of 4.5 – 6 GeV, 6 – 10 GeV, and  $> 10$  GeV by equating the sum of the computed values for the five annular bins to 100. The derived PSF profiles are shown in Table 5.

To validate the usage of the approximate PSF for the search for pair halos presented in Sect. 3.2, we verify that the PSF obtained using the method developed in the current Section is similar to that obtained by stacking spatial distributions of  $\gamma$  rays recorded during AGN flares as done in Sect. 3.1 (see Table A2). Both the reconstructed PSFs are shown in Table 5. We checked and found that these reconstructed PSFs agree within the statistical error bars. As further validation, we re-wrote the stacked distributions of photons (after subtraction of a background) for quiescent states for each selected redshift interval (see Table A4) in

**Table 5.** The PSF profiles derived from the analysis of 158 flaring sources by using the method developed in Sect. 4.2 and from only flares (see Sect. 3.1), and from the Crab pulsar data

Annular bin	Energy bands		
	4.5 – 6 GeV	6 – 10 GeV	$> 10$ GeV
Method from Sect. 4.2	-	-	-
$0^\circ < r < 0^\circ.21$	$61.8 \pm 3.8$	$69.8 \pm 3.9$	$79.4 \pm 4.8$
$0^\circ.21 < r < 0^\circ.3$	$19.6 \pm 2.1$	$14.6 \pm 1.7$	$9.9 \pm 1.7$
$0^\circ.3 < r < 0^\circ.42$	$11.8 \pm 1.6$	$9.1 \pm 1.1$	$6.5 \pm 1.4$
$0^\circ.42 < r < 0^\circ.52$	$3.7 \pm 1.0$	$5.0 \pm 0.6$	$3.4 \pm 0.9$
$0^\circ.52 < r < 0^\circ.6$	$3.0 \pm 0.8$	$1.6 \pm 0.6$	$0.8 \pm 0.5$
Method from Sect. 3.1	-	-	-
$0^\circ < r < 0^\circ.21$	$60.9 \pm 2.6$	$68.5 \pm 2.6$	$78.8 \pm 3.2$
$0^\circ.21 < r < 0^\circ.3$	$19.0 \pm 1.5$	$15.9 \pm 1.3$	$8.9 \pm 1.1$
$0^\circ.3 < r < 0^\circ.42$	$13.0 \pm 1.2$	$9.3 \pm 1.0$	$6.6 \pm 1.0$
$0^\circ.42 < r < 0^\circ.52$	$4.4 \pm 0.7$	$4.3 \pm 0.7$	$3.8 \pm 0.8$
$0^\circ.52 < r < 0^\circ.6$	$2.6 \pm 0.6$	$2.0 \pm 0.5$	$1.8 \pm 0.6$
From the Crab pulsar data	-	-	-
$0^\circ < r < 0^\circ.21$	$57.2 \pm 2.1$	$67.0 \pm 2.2$	$81.2 \pm 2.4$
$0^\circ.21 < r < 0^\circ.3$	$17.9 \pm 1.1$	$15.4 \pm 1.1$	$9.2 \pm 0.8$
$0^\circ.3 < r < 0^\circ.42$	$14.8 \pm 1.1$	$11.4 \pm 0.9$	$5.8 \pm 0.7$
$0^\circ.42 < r < 0^\circ.52$	$6.7 \pm 0.7$	$3.4 \pm 0.5$	$2.3 \pm 0.4$
$0^\circ.52 < r < 0^\circ.6$	$3.4 \pm 0.5$	$2.7 \pm 0.5$	$1.4 \pm 0.4$

the form of Table 4 and found that the PSF profiles agree with the obtained stacked distributions of photons for quiescent states within error bars. We also re-calculated the upper limits for the fraction of gamma rays attributable to a pair halo component using the PSFs obtained in the current Section and found that the re-calculated upper limits are close to those reported in Sect. 3.2<sup>15</sup>.

## 5 COMPARISON OF METHODS TO RECONSTRUCT THE FERMI-LAT PSF

In this Section, first we compare the PSF computed by using the method developed in Sect. 4 with the PSF provided by the *Fermi*-LAT collaboration for an analysis of Pass 7 Reprocessed Fermi dataset. Furthermore, we compare the PSF computed above with that obtained by using the Crab pulsar and nebula.

<sup>15</sup> The re-calculated 95% upper limits for the fraction of gamma rays from the stacked AGN sample attributable to a pair halo component + a background in the first annular bin for the redshift interval of  $z < 0.2$ , equal 16% for the energy band of 4.5-6 GeV, 9% for the energy band of 6-10 GeV, and 7% for the energy band of  $> 10$  GeV. For the redshift interval of  $0.2 < z < 0.6$ , we found that these upper limits equal 14% for the energy band of 4.5-6 GeV, 10% for the energy band of 6-10 GeV, and 10% for the energy band of  $> 10$  GeV. For the redshift interval of  $0.6 < z < 1.3$ , we found that these upper limits equal 17% for the energy band of 4.5-6 GeV, 19% for the energy band of 6-10 GeV, and 12% for the energy band of  $> 10$  GeV. Finally, for the redshift interval of  $1.3 < z$ , we found that these upper limits equal 23% for the energy band of 4.5-6 GeV, 21% for the energy band of 6-10 GeV, and 16% for the energy band of  $> 10$  GeV. Therefore these facts validate the usage of the approximate PSFs for the searches for pair halos presented in Sect. 3.2 and the results of these searches including the upper limits on the fraction of photons attributable to a pair halo component.

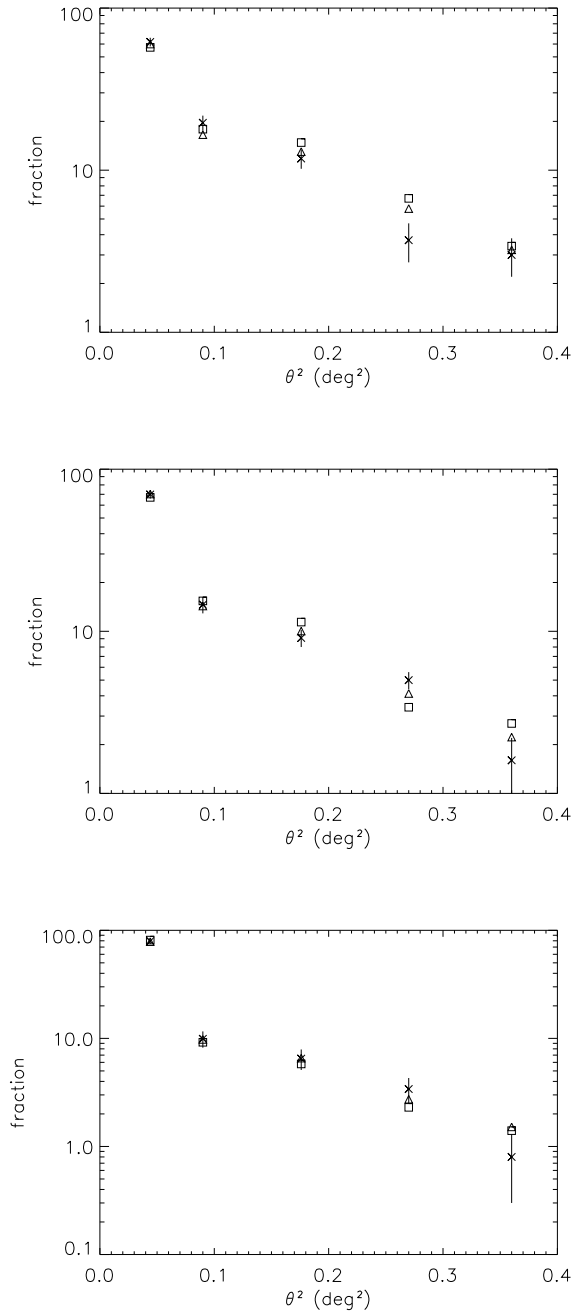


**Figure 1.** The best-fit values of fractions (the sum of the fractions over the five annular bins equals 100) obtained by modelling (triangles), the observed values with error bars computed by using AGN flares (crosses), and the central values of fractions obtained from the observations of Crab (squares). The upper panel is for the energy band of 4.5–6 GeV, the middle panel is for the energy band of 6–10 GeV, and the bottom panel is for  $> 10$  GeV.

### 5.1 Released P7REP\_SOURCE IRF PSF

In the P7REP\_SOURCE\_V15 instrument response functions (IRFs) the PSF is derived from flight data and are provided by the *Fermi*-LAT team. The updated instrument calibrations used to produce the P7REP data release improve the LAT PSF above 3 GeV, resulting in a better over-

all agreement between the Monte Carlo (MC) PSF model and the angular distributions of gamma-ray point sources. However the MC PSF was still found to slightly underestimate the PSF width above 3 GeV<sup>16</sup>. The LAT team has derived a new on-orbit PSF for P7REP data (included in the P7REP\_V15 IRFs) by rescaling the MC PSF model to match the angular distribution of Vela below 10 GeV and the stacked distribution of bright, high-latitude blazars above 10 GeV. In order to provide an independent validation of the P7REP\_SOURCE PSF for an analysis of point sources with the Fermi Science Tools<sup>17</sup>, we perform a comparison of the PSF derived in Sect. 4.2 with the P7REP\_SOURCE PSF released by the LAT team.

Using the routine, *gtmodel*, we model a point source using the P7REP\_SOURCE\_V15 IRFs for three energy bands, 4.5–6, 6–10, and  $> 10$  GeV. To compare the PSF derived in Sect. 4.2 with that modelled for a point source, we compute a normalisation factor for a modelled point source by minimising the  $\chi^2$  value. Note that we use the 5 annular bins described in Sect. 3. In Fig.1, we show the best-fit values of fractions (the sum of the fractions over the five annular bins equals 100) obtained by modelling (triangles) and the observed values with error bars computed by using the method developed in Sect. 4. The observed and modelled distributions look very similar in Fig.1. To quantitatively assess the quality of the best fits, we computed the  $\chi^2$  values and found the  $\chi^2$  values equal 7.4, 3.9, and 2.6 at 4 d.o.f. for the three energy bands, 4.5–6, 6–10, and  $> 10$  GeV, respectively. Therefore, no significant deviations of the modelled spatial distribution from the spatial distribution computed by using the procedure developed in Sect. 4 are found. We conclude that the method of the PSF reconstruction developed in Sect. 4 independently validates the usage of the P7REP\_SOURCE PSF.

### 5.2 PSF from the Crab pulsar data

The  $\gamma$ -ray signal from the bright galactic gamma-ray source at the location of the Crab pulsar in the Fermi energy band consists of two contributions: emission from the pulsar and from the associated pulsar wind nebula (PWN). Neronov et al. (2011) noticed that the size of the associated PWN is below the angular resolution of the LAT telescope onboard Fermi and proposed the Crab pulsar for the *Fermi*-LAT PSF calibration.

We applied the same data reduction procedures to the data for the region of the Crab pulsar and accumulated events for the same time interval described in Sect. 2. The distribution of photons in annular bins for three energy bands are presented in Table A6. Note that the Crab pulsar provides us with a higher number of photons than that provided by AGN flares.  $\gamma$ -ray flares computed above for our sample of AGNs and accumulated during 5.2 years provide us with the number of photons which corresponds to  $\simeq 3.5$  years of the Crab pulsar observation with *Fermi*-LAT. In Table 5, we show the PSF profiles derived from the Crab pulsar data (the sum of the fractions over the five annular bins for

<sup>16</sup> [http://fermi.gsfc.nasa.gov/ssc/data/analysis/LAT\\_caveats.html](http://fermi.gsfc.nasa.gov/ssc/data/analysis/LAT_caveats.html)

<sup>17</sup> <http://fermi.gsfc.nasa.gov/ssc/data/analysis/>

each energy band equals 100). We checked and found that the PSF profiles derived from the Crab pulsar data agree well with those that are derived by using the method developed in Sect. 4. The future observations with *Fermi*-LAT are important for a further comparison of the PSFs which are reconstructed with these two different methods. Note that 10 years of *Fermi*-LAT observations and better event reconstruction algorithms (resulting in a higher effective area) are expected to make error bars tighter by a factor of  $\approx 2$ .

## 6 CONCLUSION

We developed a method to search for pair halos through a temporal analysis of AGN emission. Our method is based on an analysis of the spatial distributions of photons coming from AGN flares and from AGN quiescent states, and a further comparison of these two spatial distributions.

To apply the method to the *Fermi*-LAT data, we selected 394 AGNs for our study. We found flaring activity in 158 AGNs of our sample. Performing the stacking of the selected AGNs, we found that the ratios of the number of photons coming from AGNs with known redshifts (sorted in the four redshift intervals) and detected during quiescent states to the number of photons coming from AGNs and detected during flares in annular bins are within the error bars for each of the three energy bands (4.5 – 6 GeV, 6 – 10 GeV, and  $> 10$  GeV) and, therefore, no evidence for a pair halo component is found in this search. We also set the 95% upper limit for the fraction of  $\gamma$  rays from the stacked AGN quiescent states for each redshift interval attributable to a pair halo component in the annular bin of  $r < 0.21^\circ$ .

We presented our method for the reconstruction of the *Fermi*-LAT PSF by using the observations of AGN flares and quiescent states (see Sect. 4). We compare the computed PSF with that obtained by using the *Fermi*-LAT dataset for the Crab pulsar. We found that both the PSFs are in good agreement. Furthermore, we applied the method of the PSF reconstruction developed in this paper to independently validate the usage of the P7REP\_SOURCE IRF PSF released by the *Fermi*-LAT team.

## ACKNOWLEDGEMENTS

Computations were performed using a high performance computing cluster in the Korea Astronomy and Space Science Institute. We are grateful to the referees for the constructive suggestions that helped us to improve this manuscript.

## APPENDIX A:

The stacked distributions of photons in annular bins for flares and for quiescent states for each selected energy band are shown in Table A1. The calculated numbers of photons in annular bins for flares and for quiescent states for each selected energy band after subtraction of a background are shown in Table A2. The ratios of the number of photons coming from 394 AGNs and detected during quiescent states to the number of photons coming from AGNs and detected

during flares are shown in Table A3. The stacked distributions of photons in annular bins for quiescent states for each selected energy band and for each selected redshift interval are shown in Table A4. The observed numbers of photons with energies between 4.5 GeV and 6 GeV in the first two annular bins for flares and for quiescent states for the five brightest sources from our final sample are shown in Table A5. The distributions of photons in annular bins for three energy bands for the Crab pulsar are shown in Table A6.

## REFERENCES

- Abdo A. A. et al., 2010a, *ApJ*, 721, 1425  
 Abdo A. A. et al., 2010b, *ApJ*, 722, 520  
 Abdo A. A. et al., 2010c, *ApJ*, 714, L73  
 Abdo A. A. et al., 2011, *ApJ*, 734, 116  
 Ackermann M. et al., 2011, *ApJ*, 743, 171  
 Ackermann M. et al., 2014, *ApJ*, 786, 157  
 Ackermann M. et al., 2013, *ApJ*, 765, 54  
 Ackermann M. et al., 2010, *ApJ*, 721, 1383  
 Aharonian F. A., Coppi P. S., Voelk H. J., 1994, *ApJ*, 423, L5  
 Ando S., Kusenko A., 2010, *ApJ*, 722, L39  
 Atwood W. B. et al., 2009, *ApJ*, 697, 1071  
 Barbiellini G. et al., 2014, *ApJ*, 784, 118  
 Bregeon J., Charles E., M. Wood for the Fermi-LAT collaboration, 2013, ArXiv e-prints: 1304.5456  
 Ciprini S., Chaty S., 2008, *The Astronomer's Telegram*, 1864, 1  
 Cutini S., Hays E., 2009, *The Astronomer's Telegram*, 2026, 1  
 Dolag K., Kachelriess M., Ostapchenko S., Tomàs R., 2011, *ApJ*, 727, L4  
 Donato D., 2010, *The Astronomer's Telegram*, 2583, 1  
 Essey W., Ando S., Kusenko A., 2011, *Astroparticle Physics*, 35, 135  
 Fairbairn M., Rashba T., Troitsky S., 2010, *MNRAS*, 403, L6  
 Finke J. D., Razzaque S., Dermer C. D., 2010, *ApJ*, 712, 238  
 Franceschini A., Rodighiero G., Vaccari M., 2008, *A&A*, 487, 837  
 Kneiske T. M., Mannheim K., Hartmann D. H., 2002, *A&A*, 386, 1  
 Kotelnikov E., Rubtsov G., Troitsky S., 2015, *MNRAS*, 450, L44  
 Murase K., Takahashi K., Inoue S., Ichiki K., Nagataki S., 2008, *ApJ*, 686, L67  
 Neronov A., Semikoz D. V., 2009, *Phys. Rev. D.*, 80, 123012  
 Neronov A., Semikoz D. V., Tinyakov P. G., Tkachev I. I., 2011, *A&A*, 526, A90  
 Neronov A., Vovk I., 2010, *Science*, 328, 73  
 Nolan P. L. et al., 2012, *ApJS*, 199, 31  
 Plaga R., 1995, *Nature*, 374, 430  
 Ryu D., Schleicher D. R. G., Treumann R. A., Tsagas C. G., Widrow L. M., 2012, *Space Science Reviews*, 166, 1  
 Sanchez D., 2010, *The Astronomer's Telegram*, 3050, 1  
 Szostek A., 2011, *The Astronomer's Telegram*, 3329, 1  
 Tavecchio F., Ghisellini G., Foschini L., Bonnoli G., Ghirlanda G., Coppi P., 2010, *MNRAS*, 406, L70

**Table A1.** The stacked distributions of photons in annular bins for flares and for quiescent states for each selected energy band.

Annular bin	State	Energy bands		
		4.5 – 6 GeV	6 – 10 GeV	> 10 GeV
0° <r< 0°.21	flare	574	686	620
0°.21 <r< 0°.3	flare	182	162	73
0°.3 <r< 0°.42	flare	130	101	58
0°.42 <r< 0°.52	flare	49	51	36
0°.52 <r< 0°.6	flare	32	28	20
1°.0 <r< 1°.3	flare	58	61	49
0 <r< 0°.21	quiescent	3040	3881	5019
0°.21 <r< 0°.3	quiescent	1012	992	802
0°.3 <r< 0°.42	quiescent	920	1001	889
0°.42 <r< 0°.52	quiescent	702	675	644
0°.52 <r< 0°.6	quiescent	521	573	527
1°.0 <r< 1°.3	quiescent	3220	3538	3287

**Table A2.** The calculated numbers of photons in annular bins for flares and for quiescent states for each selected energy band after subtraction of a background.

Annular bin	State	Energy bands		
		4.5 – 6 GeV	6 – 10 GeV	> 10 GeV
0° <r< 0°.21	flare	570±24	682±26	617±25
0°.21 <r< 0°.3	flare	178±14	158±13	70±9
0°.3 <r< 0°.42	flare	122±11	93±10	52±8
0°.42 <r< 0°.52	flare	41±7	43±7	30±6
0°.52 <r< 0°.6	flare	24±6	20±5	14±5
0 <r< 0°.21	quiescent	2830±55	3650±62	4805±71
0°.21 <r< 0°.3	quiescent	802±32	761±32	588±29
0°.3 <r< 0°.42	quiescent	500±30	540±32	460±31
0°.42 <r< 0°.52	quiescent	282±26	214±27	216±26
0°.52 <r< 0°.6	quiescent	101±23	112±25	98±24

**Table A3.** The ratios of the number of photons coming from 394 AGNs and detected during quiescent states to the number of photons coming from AGNs and detected during flares

Annular bin	Energy bands		
	4.5 – 6 GeV	6 – 10 GeV	> 10 GeV
0° <r< 0°.21	5.0 ± 0.2	5.4 ± 0.2	7.8 ± 0.3
0°.21 <r< 0°.3	4.5 ± 0.4	4.8 ± 0.4	8.4 ± 1.1
0°.3 <r< 0°.42	4.1 ± 0.5	5.8 ± 0.7	8.9 ± 1.5
0°.42 <r< 0°.52	6.9 ± 1.3	5.0 ± 1.0	7.3 ± 1.7
0°.52 <r< 0°.6	4.2 ± 1.4	5.6 ± 2.0	7.2 ± 3.0
0°.21 <r< 0°.6	4.5 ± 0.3	5.0 ± 0.3	8.2 ± 0.8

**Table A4.** The stacked distributions of photons in annular bins for quiescent states for each selected energy band and for each selected redshift interval.

Redshift	Annular bin	Energy bands		
		4.5 – 6 GeV	6 – 10 GeV	> 10 GeV
$z < 0.2$	$0^\circ < r < 0^\circ.21$	504	752	1346
$z < 0.2$	$0^\circ.21 < r < 0^\circ.3$	165	163	181
$z < 0.2$	$0^\circ.3 < r < 0^\circ.42$	118	132	165
$z < 0.2$	$0^\circ.42 < r < 0^\circ.52$	79	89	104
$z < 0.2$	$0^\circ.52 < r < 0^\circ.6$	47	50	57
$z < 0.2$	$1^\circ.0 < r < 1^\circ.3$	294	339	327
$0.2 < z < 0.6$	$0^\circ < r < 0^\circ.21$	546	666	836
$0.2 < z < 0.6$	$0^\circ.21 < r < 0^\circ.3$	173	147	133
$0.2 < z < 0.6$	$0^\circ.3 < r < 0^\circ.42$	150	168	131
$0.2 < z < 0.6$	$0^\circ.42 < r < 0^\circ.52$	120	113	110
$0.2 < z < 0.6$	$0^\circ.52 < r < 0^\circ.6$	78	102	94
$0.2 < z < 0.6$	$1^\circ.0 < r < 1^\circ.3$	461	472	497
$0.6 < z < 1.3$	$0 < r < 0^\circ.21$	639	784	765
$0.6 < z < 1.3$	$0^\circ.21 < r < 0^\circ.3$	216	227	135
$0.6 < z < 1.3$	$0^\circ.3 < r < 0^\circ.42$	202	197	154
$0.6 < z < 1.3$	$0^\circ.42 < r < 0^\circ.52$	149	138	121
$0.6 < z < 1.3$	$0^\circ.52 < r < 0^\circ.6$	107	132	104
$0.6 < z < 1.3$	$1^\circ.0 < r < 1^\circ.3$	703	741	681
$1.3 < z$	$0 < r < 0^\circ.21$	333	311	271
$1.3 < z$	$0^\circ.21 < r < 0^\circ.3$	121	89	51
$1.3 < z$	$0^\circ.3 < r < 0^\circ.42$	120	116	88
$1.3 < z$	$0^\circ.42 < r < 0^\circ.52$	98	95	68
$1.3 < z$	$0^\circ.52 < r < 0^\circ.6$	76	74	58
$1.3 < z$	$1^\circ.0 < r < 1^\circ.3$	464	476	438

**Table A5.** The observed numbers of photons with energies between 4.5 GeV and 6 GeV in the first two annular bins for flares and for quiescent states for the five brightest sources from our final sample.

Source name	State	Energy band	Annular bins		Number of intervals
			$0^\circ < r < 0^\circ.21$	$0^\circ.21 < r < 0^\circ.42$	
4C +21.35	flare	4.5-6 GeV	51	34	60
3C 279	flare	4.5-6 GeV	21	13	40
PKS 1510-08	flare	4.5-6 GeV	56	22	80
PKS 0537-441	flare	4.5-6 GeV	34	16	51
Mkn 421	flare	4.5-6 GeV	17	7	20
4C +21.35	quiescent	4.5-6 GeV	32	21	633
3C 279	quiescent	4.5-6 GeV	49	21	497
PKS 1510-08	quiescent	4.5-6 GeV	73	44	1052
PKS 0537-441	quiescent	4.5-6 GeV	106	48	858
Mkn 421	quiescent	4.5-6 GeV	228	110	1206
4C +21.35	flare	6-10 GeV	65	22	60
3C 279	flare	6-10 GeV	17	9	40
PKS 1510-08	flare	6-10 GeV	49	20	80
PKS 0537-441	flare	6-10 GeV	62	17	51
Mkn 421	flare	6-10 GeV	36	9	20
4C +21.35	quiescent	6-10 GeV	42	10	633
3C 279	quiescent	6-10 GeV	36	21	497
PKS 1510-08	quiescent	6-10 GeV	83	32	1052
PKS 0537-441	quiescent	6-10 GeV	140	46	858
Mkn 421	quiescent	6-10 GeV	364	133	1206

**Table A6.** The distributions of photons in annular bins for three energy bands for the Crab pulsar.

Quantity	Annular bin	Energy bands		
		4.5 – 6 GeV	6 – 10 GeV	> 10 GeV
Photons	$0^\circ < r < 0^\circ.21$	782	948	1118
Photons	$0^\circ.21 < r < 0^\circ.3$	247	220	129
Photons	$0^\circ.3 < r < 0^\circ.42$	208	164	85
Photons	$0^\circ.42 < r < 0^\circ.52$	98	51	37
Photons	$0^\circ.52 < r < 0^\circ.6$	54	41	24
Photons	$1^\circ.0 < r < 1^\circ.3$	56	35	37